

Low-Cycle Fatigue Behavior and Fracture Mechanism of HS80H Steel at Different Strain Amplitudes and Mean Strains

Wenlan Wei, Lihong Han, Hang Wang, Jianjun Wang, Jianxun Zhang, Yaorong Feng, and Tao Tian

(Submitted June 27, 2016; in revised form January 16, 2017; published online February 24, 2017)

This work studied the low-cycle fatigue (LCF) behavior of HS80H steel at room temperature. LCF tests at strain amplitudes of 0.4, 0.6, 0.8, 1.0, 1.2, 1.6, and 2.0% were conducted under constant mean strain. In addition, tests at mean strains of -0.8 , -0.3 , 0, 0.5, and 1.2% were conducted under constant strain amplitude. The microstructure and fracture surface of the material after the tests were characterized using scanning electron microscopy and transmission electron microscopy, respectively. Results of LCF test demonstrate the hardening-softening transition of HS80H steel. And it is associated with strain amplitude and mean strain. In addition, LCF life is affected by strain amplitude and mean strain. In asymmetric fatigue, the maximum absolute value of strain and fatigue life displays a linear relationship in double logarithmic coordinates. Microscopic observation showed that fatigue crack propagates through transgranular propagation resulting from the interaction between dislocation pileup and precipitates.

Keywords cracks, fracture mechanism, low-cycle fatigue behavior, mean strain

1. Introduction

HS80H steel is a type of tempered martensite steel that is used for thermal recovery well casing. Strength is an important mechanical parameter to consider in designing a casing material for conventional wells. However, new problems have been encountered in thermal recovery wells. Failure usually occurs following thermal recovery cycles in casing, which is designed according to strength parameters (Ref 1-3). Thus, previous designs do not satisfy the working environment of thermal recovery wells (Ref 4-7). Given the particularity of service environment, a thermal recovery well demonstrates a working environment with a significant low-cycle fatigue (LCF) (Ref 8, 9). Therefore, the LCF property of a casing material is the key property of a thermal recovery well.

Strain amplitude and mean strain are two important control parameters in LCF test. In previous studies, tests were usually performed in accordance with symmetrical fatigue, in which the mean strain is zero. The fatigue life is then determined by the magnitude of the strain amplitude (Ref 10, 11). In the working environment of thermal recovery well, working conditions are not just tension-compression cycle. Some plastic deformations usually occur prior to the tension-compression cycle. In other words, the mean strain is not zero. Some experimental results

show that the mean strain can significantly reduce the LCF life (Ref 12). Moreover, numerous explanations have been provided for the damage caused by mean strain. The mean strain increases the maximum strain, leading to crack initiation. Then, the crack can be extended under small load (Ref 13). In LCF, tempered martensite steel demonstrates hardening-softening phenomenon (Ref 14). The tension-compression cycle causes the migration of dislocations. This process leads to dislocation accumulation, forming a dislocation pileup. Therefore, this may be one of the reasons for the material to demonstrate cyclic hardening and then cyclic softening. Several studies have investigated the microstructure after fatigue. Studies have indicated that dislocation always moves toward the grain boundary (Ref 15-17).

Studies on tempered martensite steel have mostly focused on the steel, such as P91 and P92, of pressure vessels. The Cr content of the steel is usually approximately 9%. The casing steel is a high-manganese steel that contains only small amounts of Cr and Mo. The LCF behavior of casing steel is rarely investigated. This work investigated the effects of strain amplitudes and mean strain on LCF life. In addition, the fracture mechanism was explored.

2. Experimental

HS80H steel was used in the present investigation, and its chemical compositions are listed in Table 1. HS80H steel, which is a type of martensitic steel tempered at 650 °C, is on the basis of the original composition of N80 steel (Ref 18).

The samples used for LCF tests were cylindrical. The diameter of the sample was 6 mm, and the gauge was 12 mm. Strain-controlled fatigue tests were conducted at a room temperature by using a closed-loop servo hydraulic testing machine (Ref 19). And the tests employed tension-compression fatigue loading. The samples were divided into two groups. In the first group, strain amplitude was variable and the mean

Wenlan Wei and Jianxun Zhang, State Key Laboratory for Mechanical Behavior of Materials, Xi'an Jiaotong University, Xi'an 710049, People's Republic of China; and Lihong Han, Hang Wang, Jianjun Wang, Yaorong Feng, and Tao Tian, State Key Laboratory of Performance and Structural Safety for Petroleum Tubular Goods and Equipment Materials, Xi'an 710065 Shaanxi, People's Republic of China. Contact e-mail: weiwlannds@163.com.

Table 1 Chemical compositions of HS80H steels (wt.%)

C	Si	Mn	P	S	Cr	Mo	Ni	V	Ti	Cu
0.17	0.24	0.98	0.011	0.0034	0.99	0.33	0.059	0.029	0.013	0.021

Table 2 Test result of LCF for HS80H steels

No.	ε_a , %	$\varepsilon_{\text{mean}}$, %	R	N_f , cycles
First group				
G11	0.4	0.0	-1	...
G12	0.6	0.0	-1	988
G13	0.8	0.0	-1	526
G14	1.0	0.0	-1	305
G15	1.2	0.0	-1	178
G16	1.6	0.0	-1	124
G17	2.0	0.0	-1	68
Second group				
G21	1.0	-0.8	-9.00	230
G22	1.0	-0.3	-1.86	297
G23	1.0	0.0	-1.00	305
G24	1.0	0.5	-0.33	239
G25	1.0	1.2	0.09	186

strain was constant (mean strain = 0%). A triangular strain waveform with seven strain amplitudes, namely 0.4, 0.6, 0.8, 1.0, 1.2, 1.6, and 2.0%, was used at a constant total strain rate of $4 \times 10^{-3} \text{ s}^{-1}$. In the second group, the mean strain was variable and the strain amplitude was constant (strain amplitude = 1%). And strain rate and waveform were consistent with those in the first group. The mean strains selected were -0.8, -0.3, 0, 0.5, and 1.2%. Then, the sample was defined as a failure when the cyclic loading dropped to 75% from the maximum.

The characteristics of the microstructure and fracture surface of HS80H steel after the LCF test were observed by scanning electron microscopy (SEM) and transmission electron microscopy (TEM), respectively. The samples used for SEM observation were treated as follows: The fracture surfaces were cleaned through ultrasonic cleaning in the acetone solution. Samples for microstructure observation were cut from the failure sample using wire-electrode cutting machine (i.e., longitudinal section from fracture and surface cracks). Then, the samples were etched for 10 s in a solution containing 4% nitric acid and alcohol after grinding. The samples used for TEM were obtained through wire-electrode cutting and thinned to 30-50 μm by using sandpaper. Then, the samples were observed under TEM after twin-jet electropolishing.

3. Results and Discussion

Table 2 shows the results of LCF test, which contains strain amplitudes (ε_a), mean strain ($\varepsilon_{\text{mean}}$), strain ratio (R) and failure cycle (N_f), for the two groups. G14 and G23 are the same samples. Mean strains are defined as follows:

$$\varepsilon_{\text{mean}} = \frac{\varepsilon_{\text{max}} + \varepsilon_{\text{min}}}{2} \quad (\text{Eq 1})$$

where ε_{max} and ε_{min} are the maximum and minimum strains, respectively.

3.1 Cyclic Hardening and Softening

Figure 1(a) shows the peak tensile stress of different strain amplitude-cycle curves under a constant mean strain of 0%. Seven strain amplitudes are used from 0.4 to 2.0%. As the strain amplitude is increased, the fatigue life decreases. In the initial phase of LCF, four curves displayed an obvious hardening phenomenon and softening trend at 1.0, 1.2, 1.6, and 2.0% strains. In addition, the two curves showed softening, hardening, and another softening behavior at 0.8 and 0.6% strains. The curve with 0.4% strain continuously softened, and the test was disrupted caused by instability. After hardening, the softening stage began, and the peak tensile stress steadily decreased with the increase in cycles. When peak tensile stress began to decrease rapidly, the sample was about to fail.

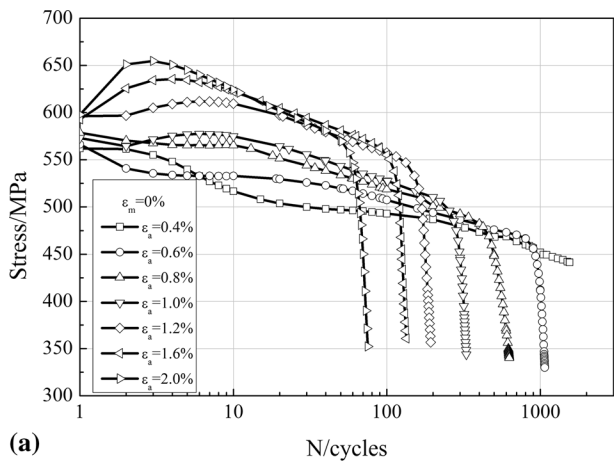
Figure 1(b) shows the peak tensile stress of different average strain-number of cycles curves under a constant strain amplitude of 1.0%. To facilitate observation, a linear axis was used in the x-axis to represent the number of cycles caused by the different mean strains, which did not show remarkable difference compared with number of cycles caused by the different strain amplitudes. The second group also demonstrated hardening phenomenon and then softening trend at the initial phase of testing (Fig. 1b, upper right corner). Figure 1(b) shows that cyclic hardening obvious varies under different mean strains.

The peak tensile stress rate of change can be used to describe hardening-softening transitions. Peak tensile stress rate of change is defined as follows:

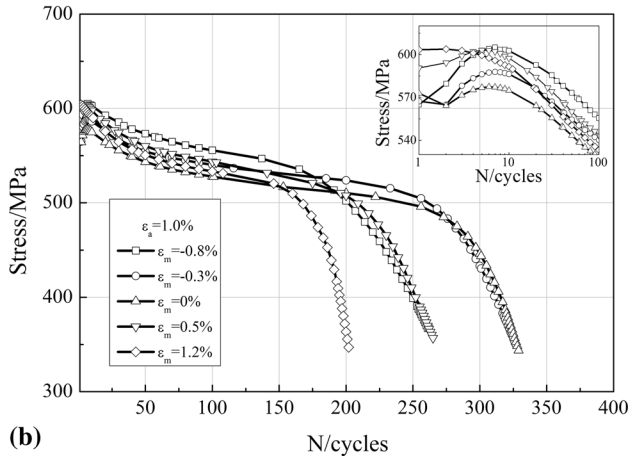
$$v_{\sigma} = \Delta\sigma / \Delta n \quad (\text{Eq 2})$$

where $\Delta\sigma$ is the difference between two peak values of tensile stress, and Δn is the cycle number between two peak tensile stress values.

A positive rate of change indicates increasing peak tensile stress, whereas a negative rate of change indicates decreasing peak tensile stress. Figure 2(a) shows the rate of change in peak tensile stress at $\varepsilon_a = 2.0\%$ and $\varepsilon_m = 0\%$. The stress increased



(a)



(b)

Fig. 1 Peak tensile stress-cycles curve on (a) strain amplitudes and (b) mean strain

initially and then decreased; the critical point of positive-negative conversion is the transition point for hardening-softening. Then, the observations at 1.0, 1.2, and 1.6% strains are similar to that at 2.0% strain. Figure 2(b) shows the rate of change in peak tensile stress at $\epsilon_a = 0.6\%$ and $\epsilon_m = 0\%$. The stress initially decreased, stabilized, slightly increased, and then decreased again. Then, the observation at 0.8% strain is similar to that at 0.6% strain. Figure 2(c) and (d) shows the rate of change in peak tensile stress at $\epsilon_m = -0.8\%$ and $\epsilon_m = 1.2\%$ under $\epsilon_a = 1.0\%$. The trend of the curve with different mean strains is consistent with Fig. 2(a).

The transition points of hardening-softening are shown in Fig. 3. Then, it can be inferred that the cycle number of hardening-softening transition decreased with increasing strain amplitudes and mean strains. Cyclic hardening is considered to be caused by dislocation pileup effect in tempered martensite steel (Ref 20, 21). Experimental results show that the pileup effect of dislocation weakened with decreasing strain amplitude. However, when the mean strain was negative, the absolute value of the strain amplitude increased and the cycle number of hardening-softening transition did not decrease. Thus, it can be concluded that the tensile strain plays a leading role in the cyclic hardening effect in the initial stage of LCF in HS80H steel. When the tensile strain is large, the maximum value of hardening is reached more rapidly.

The cyclic hardening ratio and cyclic softening ratio are used to compare the effects of different strains on cyclic hardening and cyclic softening. These ratios are defined as follows:

$$R_{\text{Hardening}} = \frac{\sigma_{\text{max}}}{\sigma_{\text{ex}}} - 1 \quad (\text{Eq 3})$$

$$R_{\text{Softening}} = 1 - \frac{\sigma_{0.5N_f}}{\sigma_{\text{max}}} \quad (\text{Eq 4})$$

where σ_{max} is peak tensile stress of transition point of hardening-softening, σ_{ex} is the minimum peak tensile stress before transition point of hardening-softening, and $\sigma_{0.5N_f}$ is the peak tensile stress at the half-life of the fatigue.

Figure 4 shows the results of cyclic hardening and cyclic softening ratios at different strain amplitudes and mean strains. The straight line in the graph is obtained from the linear regression of the scatter plot. Figure 4(a) shows the cyclic hardening ratio. The two straight lines in the graph show the cyclic hardening ratio of different strain amplitudes and mean strains. Then, it can be concluded that the cyclic hardening ratio increased with increasing strain amplitude. When the strain amplitude is 0.6%, the hardening ratio approximates zero. In the test results, cyclic hardening did not appear at strain amplitude of 0.4%. The effect of mean strain on cyclic hardening ratio showed the opposite trend which the cyclic hardening ratio decreased with increasing mean strain. Obvious differences can be found in the slope of the two straight lines. The influence of strain amplitude on the cyclic hardening ratio is more significant than that of the mean strain. Figure 4(b) shows the cyclic softening ratio. And the effect of strain amplitude and mean strain on the cyclic softening remains different. The cyclic softening ratio increases with increasing mean strain, and the strain amplitude does not significantly affect the cyclic softening ratio.

In summary, HS80H steel under LCF presents a hardening-softening transition. However, the cause of hardening in the macro scope cannot be explained. Section 3.3 discusses the microscopic aspect.

3.2 Fatigue Life

The strain-life curves of LCF are usually expressed in half amplitude ($\Delta\epsilon/2$) of the total strain and reversals to failure ($2N_f$) in the double logarithmic coordinates (Ref 22, 23). The half amplitude of the total strain is divided into elastic strain and plastic strain. The Manson-Coffin fatigue model is expressed as follows:

$$\epsilon_a = \frac{\sigma'_f}{E} (2N_f)^b + \epsilon'_f (2N_f)^c \quad (\text{Eq 5})$$

where ϵ_a is strain amplitude, σ'_f is fatigue strength coefficient, E is elastic modulus, b is fatigue strength exponent, ϵ'_f is the fatigue ductility coefficient, and c is the fatigue ductility exponent.

The Manson-Coffin equation fits well with the half amplitude of elastic strain and plastic strain. The relationship between the half amplitude of total strain and the reversals to failure was then obtained. The fitting coefficients and curves are shown in Table 3 and Fig. 5, respectively.

In symmetrical LCF, the mean strain is zero, and the Manson-Coffin fatigue model responds to the relationship between strain amplitude and number of cycles. In the

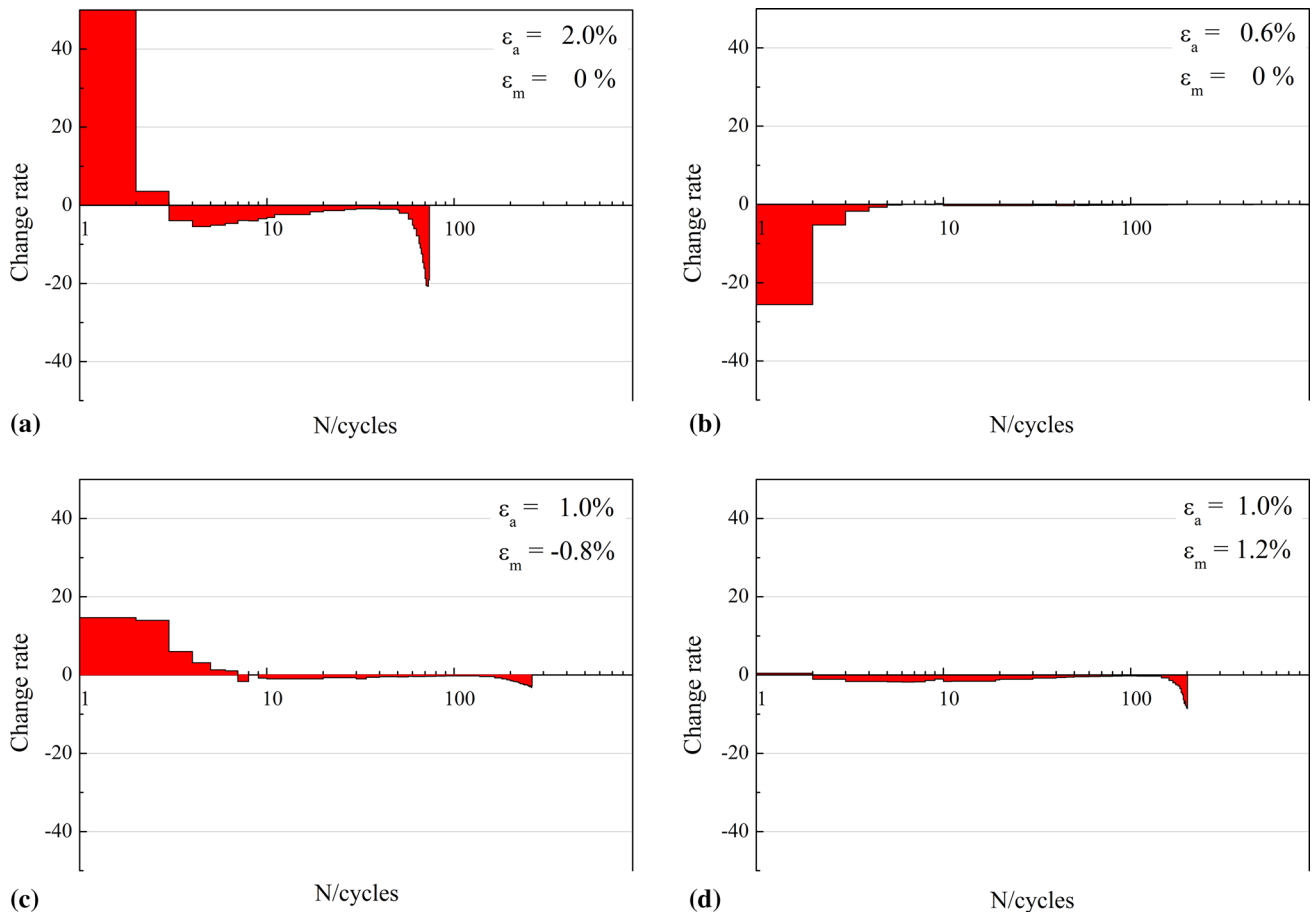


Fig. 2 Change rate of peak tensile stress-cycles curve: (a) $\epsilon_a = 2.0\%$, $\epsilon_m = 0\%$; (b) $\epsilon_a = 0.6\%$, $\epsilon_m = 0\%$; (c) $\epsilon_a = 1.0\%$, $\epsilon_m = -0.8\%$; (d) $\epsilon_a = 1.0\%$, $\epsilon_m = 1.2\%$

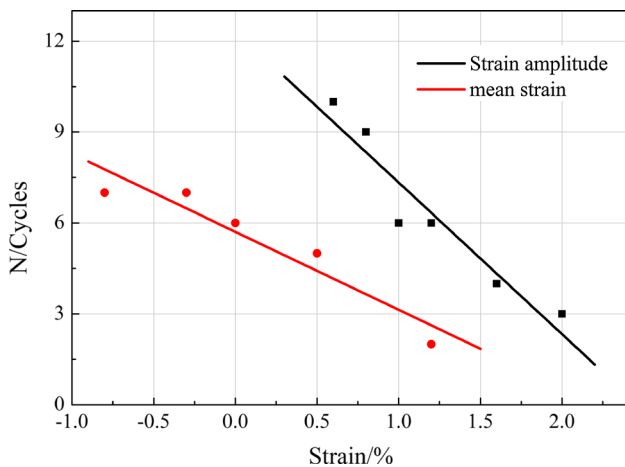


Fig. 3 Number of cyclic hardening-strains curve

asymmetric fatigue, the fatigue lives of different mean strains are similar under the same strain amplitude if calculated in accordance with the Manson-Coffin fatigue model. However, this model cannot reflect the changes in fatigue life resulting from the transformation of the mean strain. The test results from Group 2 show that the fatigue life decreased with increasing mean strain when the mean strain is greater than zero and increased with increasing mean strain when the mean strain

is less than zero. The transition point appears when the mean strain is zero. The opposite trend is observed when the mean strain is greater than or less than zero.

A method for asymmetric LCF has been proposed in the literature. The maximum strain, $\epsilon_{\max} = \epsilon_a + \epsilon_{\text{mean}}$, and number of cycles were used to fit fatigue equation according to the Manson-Coffin fatigue model (Ref 24, 25). The strain-life curves were then obtained in the asymmetric LCF. However, this method is feasible within a certain range. The half amplitude of total strain in the Manson-Coffin fatigue model is actually the maximum strain. The Maximum strain was then decomposed into elastic and plastic stages. When the mean strain is greater than zero, the tensile strain is larger than the compressive strain. In addition, the maximum strain plays a leading role in the internal damage of the material. Relatively reliable results can be obtained according to the maximum strain for fitting. When the mean strain is less than zero, the tensile strain is lower than the compressive strain. In this case, compressive strain plays a leading role in the internal damage of the material. The maximum strain is evidently unsuitable for data fitting. Therefore, when the mean strain is less than zero, the minimum strain ($\epsilon_{\min} = \epsilon_{\text{mean}} - \epsilon_a$) is selected as the fitting data. As such, the absolute value of the maximum strain or the minimum strain is selected. Fatigue damage is always dominated by the maximum amplitude of the strain. The maximum value of the absolute value of strain and number of cycles can be inferred to display linear relationship in the double

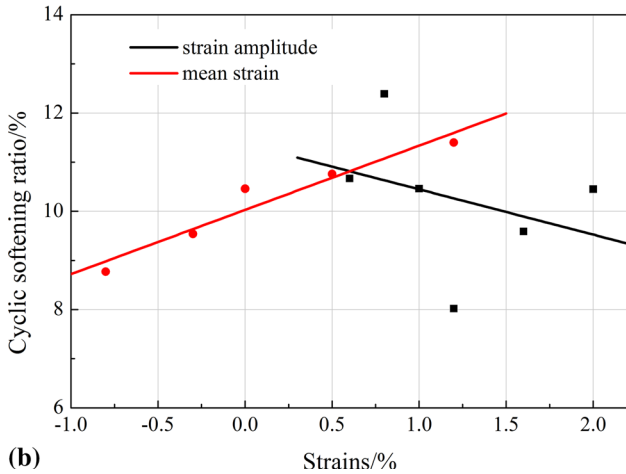
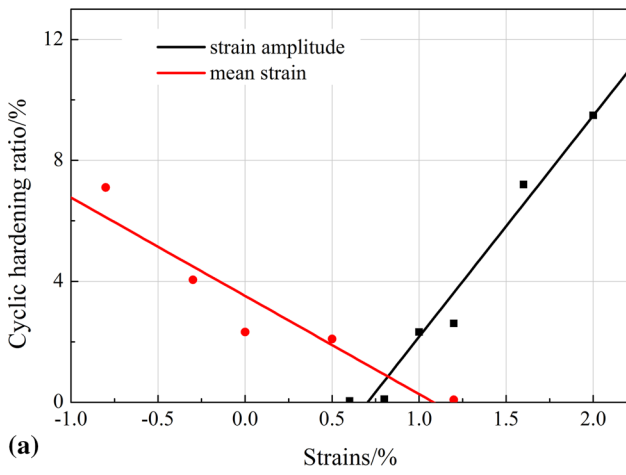


Fig. 4 Cyclic hardening ratio (a) and cyclic softening ratio (b) curve

Table 3 LCF fitting coefficients of HS80H steel from fully reversed loading

σ'_f	b	ϵ'_f	c
1037	-0.085	0.205	-0.593

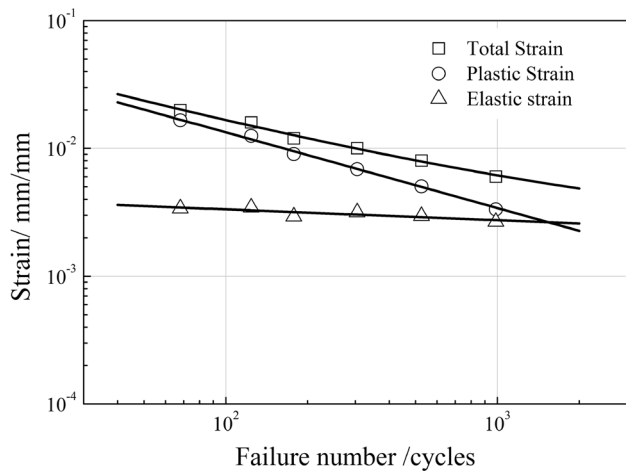


Fig. 5 Strain-life curve under the influence of strain amplitude

logarithmic coordinates. Based on the above conclusions, the following formula is used to fit the test results:

$$\epsilon_{|\max, \min|} = C(2N_f)^m \quad (\text{Eq 6})$$

where C and m are the material coefficients related to fracture ductility of material.

Figure 6 shows the fitting results. The maximum absolute values of strain are presented by blocks, the maximum strains are presented by circles, and the minimum strains are presented by delta. The line represents the fitting results, in which C is 25.27 and m is -1.35 . Obviously, no significant linear relationship exists between the maximum and minimum strains at the mean strain ranging from -0.8 to 1.2% in the double logarithmic coordinates. These strains present an irregular distribution. Then, this finding shows that taking the maximum or minimum strain separately is not appropriate. In addition, the maximum value of the absolute value of strain displays a good linear relationship, indicating the confidence of the above inference. The asymmetric LCF test results verify the leading function of the maximum absolute value in the fatigue life. In other words, the absolute value of the mean strain is related to the fatigue life under the same strain amplitude.

3.3 Characterization of Microstructure and Fractures

HS80H steel under LCF presents a hardening-softening transition. And the degree of hardening and softening is related to strain amplitude and mean strain. However, the cause of hardening in the macro scope cannot be explained. LCF properties and microstructure are closely related, and the characteristics of microstructure significantly influence the LCF. The characteristics of the microstructure determine how the material produces voids and cracks, as well as the manner of crack propagation during LCF. To study the influence of different strains and mean strain values on the fracture and the mechanism of the fracture of HS80H steel, the microstructure after fracture and fracture surface were observed and analyzed, respectively.

3.3.1 The Nucleation and Propagation of Cracks. The cross section of the original sample, which was acquired prior to the test, was analyzed using SEM (Fig. 7). Results show that the grain size is generally within $20 \mu\text{m}$. The grains display two forms, namely island and lamellar forms. Given that the grains exist in different orientations, the grains present different forms

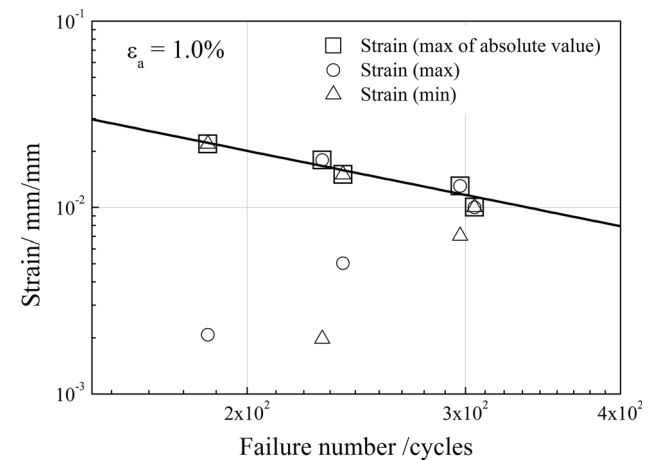


Fig. 6 Strain-life curve under the influence of mean strain

in SEM photograph (Ref 26). Moreover, the grain interior exhibits dense white spots, which are granular cementites produced through tempering at 650 °C (Ref 27). The lamellar microstructures are lath martensites composed of granular cementites and ferrite. In addition, several large white particles are carbides.

Given that the secondary electron method cannot be clearly distinguished from the grain boundary of the tempered martensite steel, the back-scattered electron method was used for observation (Fig. 8). The grain boundaries between grains with different orientations obviously vary. The portion parallel to the observation plane is bright gray, and the portion perpendicular to the observation plane is dark gray (Fig. 8a). And the lamellar form can be clearly seen in the dark gray area.

After fracture of the LCF sample, numerous cracks, in addition to the fracture surface, were observed on the sample surface. Figure 8(b) shows a crack that is not fully extended in the sample with strain amplitude of 1% and a mean strain of 1.2%. A barrier appeared on the path of crack propagation, the initial crack is terminated, and a new secondary crack is nucleated on the other path to continue crack growth (Fig. 8b). The dotted line in the figure shows the position where the initial crack is terminated on the boundaries of two grains with different orientations. It can be concluded that the grain

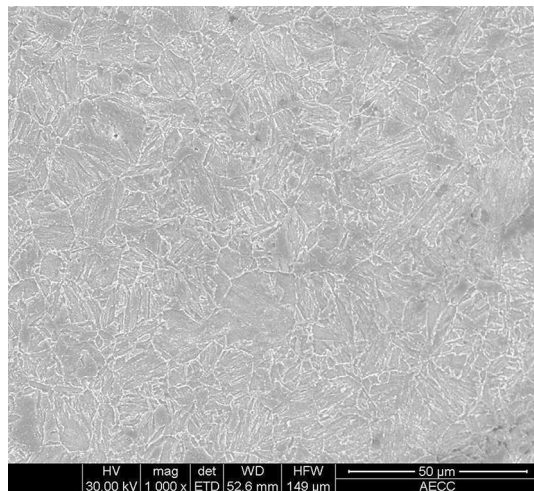


Fig. 7 Microstructure of HS80H steel under $\times 1000$

boundaries produced by the grains in different orientations can hinder crack propagation. Then, two problems are derived from this phenomenon. The first is the mechanism by which the grain boundaries produced by the grains with different orientations impede crack propagation, and the other is the mechanism of the formation of new crack.

A large number of precipitates and disordered distribution of dislocations exist in the grains of HS80H steel (Fig. 9a). During LCF loading, these dislocations move toward the grain boundaries, and the newly formed dislocations are simultaneously stacked on each other. With the increase in dislocation density, dislocation pileup forms at the grain boundary. Figure 9(b) shows the TEM morphology of the dislocation distribution of the fractured sample under the strain amplitude of 1% and a mean strain of 1.2%. The dislocation pileup is densely distributed on the grain boundaries. Then, the grain boundary between two different orientations is strengthened due to the pileup effect (Ref 28). Greater the number of dislocation pileup indicates greater resistance to crack propagation.

The section of fracture surface of the sample, at strain amplitude of 1%, and mean strain of 1.2%, was observed (Fig. 10). Figure 10(a) shows the sectional fracture of the sample after fatigue test. In addition, a secondary crack is obvious in the section. Large voids with sizes between 5 and 10 μm appeared near the path of crack propagation. And weensy voids were usually considered to appear when the sample is subjected to loading. Then, the voids gradually grow, leading to crack initiation and propagation until fracture (Ref 29, 30). Large voids were found around the crack, demonstrating that the voids had grown to the extent that they can accelerate the crack propagation and lead to fracture in the end. Figure 10(b) shows the magnified image of the secondary crack tip. And numerous tiny voids appeared in the grain interior. Several representative voids were selected and marked in the graph. Voids also appeared in the vicinity of the secondary crack tip at distances of less than 5 μm . In addition, the void around the crack is the weaker part of the grain structure. When crack growth was impeded, as shown in Fig. 8(b), the crack always extended to the weakest part of the grain. The interaction between dislocation pileups and voids terminated the main crack propagation and initiated new secondary cracks.

Figure 10(b) shows that the crack is a transgranular crack which extended through the grain structure. This phenomenon

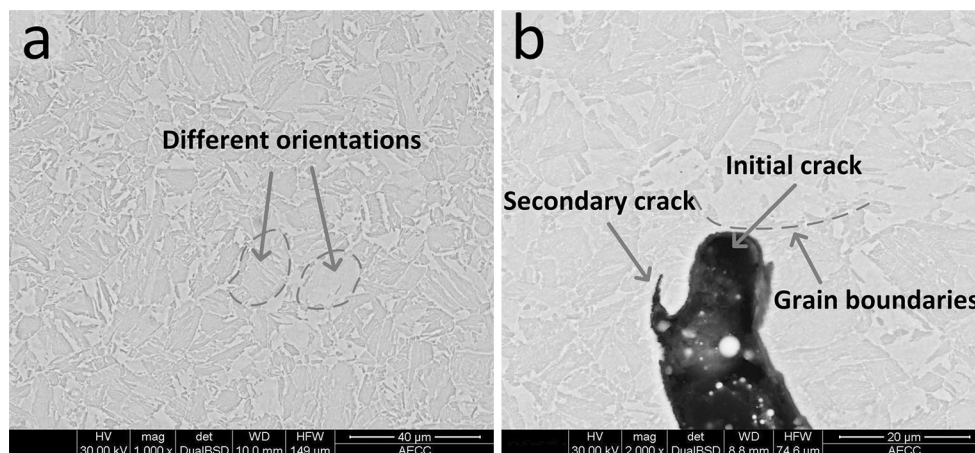


Fig. 8 Microstructure: grain boundaries (a) and barrier of crack propagation (b)

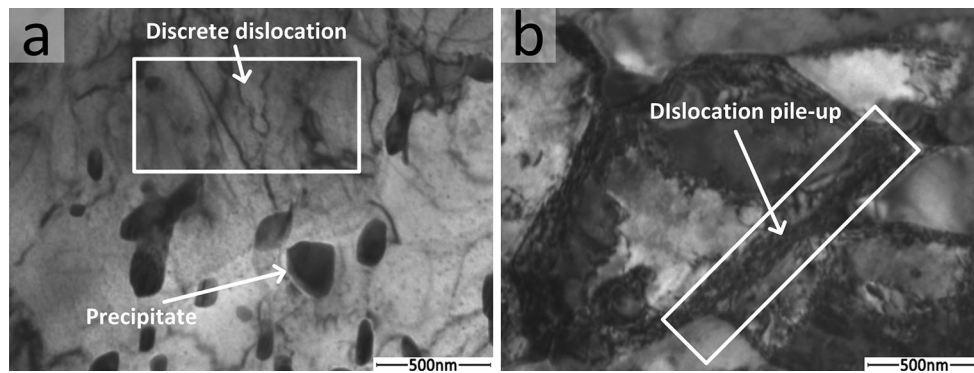


Fig. 9 TEM of original dislocations in grain (a) and grain boundaries after fatigue (b)

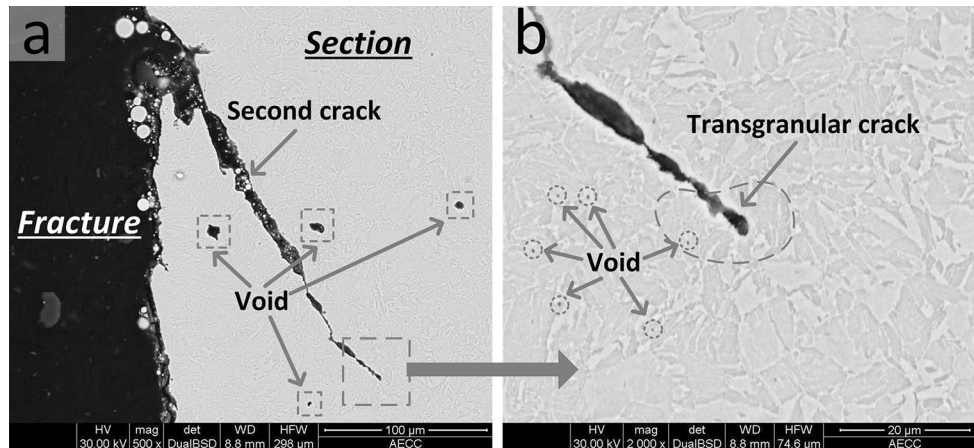


Fig. 10 SEM of (a) crack propagation and (b) voids

shows that the resistance of crack growth in the grain is less than that along the grain boundary due to the presence of voids inside the grain. Based on the SEM observations above, the process of void nucleation can be inferred. Under tensile or compressive load, the material has a certain strain. The stiffness of the precipitates inside the grains and grains differs at the microscale. Therefore, the strain of the grain should be different from that of the internal precipitates. Then, the stress concentration is generated around the precipitates, causing the internal tearing of the grains to produce microcracks. In addition, the microcracks are voids.

3.3.2 The Morphology of Fracture. The fracture surfaces of the samples were obtained from the second group of test samples with mean strains of 0 and 1.2%. In the sample with a mean strain of 0%, the lower strain limit is -1.0% , and the upper limit is 1% . In the sample with a mean strain of 1.2% , the lower strain limit is 0.2% , and the upper limit is 2.2% . The crack source, crack propagation direction, and fracture surface were analyzed.

Figure 11 shows the fracture surface with mean strain of 0% and strain amplitude of 1%. The fatigue fracture surface is divided into three parts, the left part is the final rupture area, the middle part is the crack growth area, and the right part is the crack initiation area (Fig. 11a). On the basis of the direction of crack propagation, crack initiation was found to be multi-source, and two crack sources exist. A large number of feathery fatigue striations, which constitute a typical fatigue characteristic, can be observed in the crack growth area (Ref 30). Two cracks with different crack sources are combined after a period of expansion (Fig. 11b). Given that the two crack sources are

not in the same plane, an intersection that is shaped like a step is formed. In the step region, cracks are combined along the grain direction. Cracks continue to expand after the combination and gradually achieved stable expansion. A dark gray area was observed in the stable expansion (Fig. 11c). In addition, the fatigue crack showed secondary cracks in the expansion, and these cracks were located in two relatively flat areas with a width of approximately $20\ \mu\text{m}$. The striation area after amplification displayed obviously brittle characteristics. This finding shows that the fracture mode is cleavage fracture (Fig. 11d). Ductile features were found around the brittle feature area. Given the characteristics of tension-compression cycle of LCF, brittle-ductile alternating regions appear continuously.

To compare the fatigue fracture surfaces between different mean strains, we observed the fracture surface under 1.2% mean strain and 1% strain amplitude. Only a single crack source was observed in the fracture surface of mean strain of 1.2% . Fatigue striation showed white strip from Fig. 11(c). And it presents a dense white short line in Fig. 11(a). In Fig. 12(a), the number of white short lines is obviously reduced. Namely, the number of fatigue striation is obviously less than that of low-mean strain test sample (mean strain of 0%). The crack growth area appears to contain brittle feature area with a large width of $40\text{--}60\ \mu\text{m}$ (Fig. 12b). Then, the distance between the two adjacent brittle feature areas becomes larger, indicating that the crack length in the single-cycle expansion increased. Thus, the number of cycles to produce the same crack length is reduced. The sample is assumed to fail when the crack is extended to a certain length. The longer the crack propagation

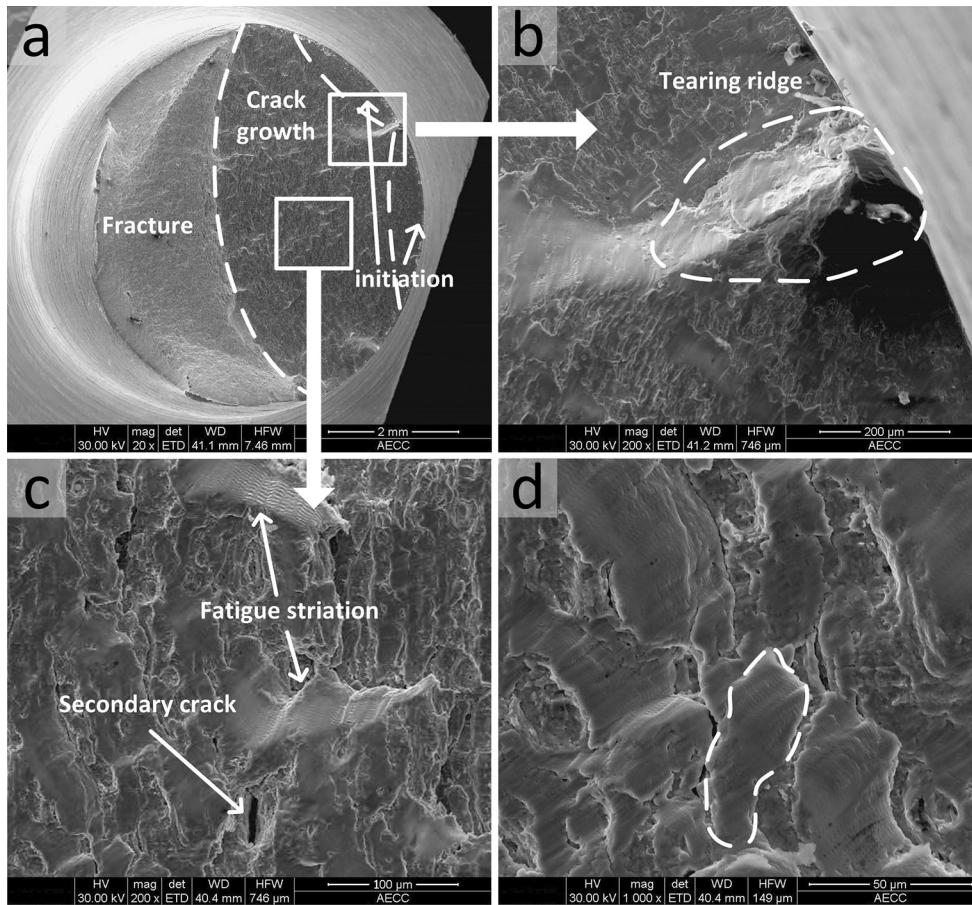


Fig. 11 Fracture surface with mean strain = 0%: (a) macroscopic fracture surface, (b) tearing ridge, (c) secondary crack and fatigue striation, (d) brittle feature

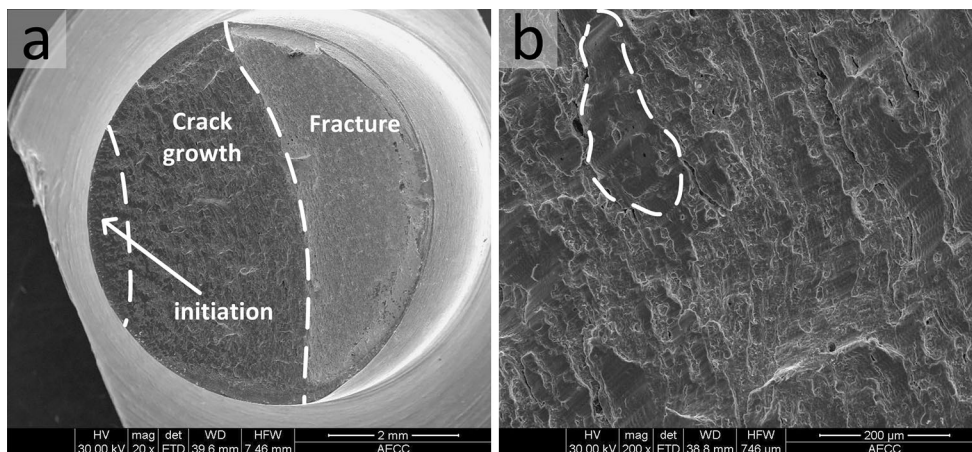


Fig. 12 Fracture surface with mean strain = 1.2%: (a) macroscopic fracture surface, (b) brittle feature

within one period, the less the fatigue life would be. Therefore, the fatigue life is reduced under high mean strain.

4. Conclusions

This work investigated the LCF behavior and fracture mechanism of HS80H steel. The effects of different strain

amplitudes and mean strains, the initiation and propagation mechanism of fatigue crack, and the fracture surface morphology of different mean strains were discussed. The conclusions drawn from the above discussion are as follows:

1. HS80H steel showed cycle hardening and then cycle softening behavior during LCF. The transition point from cycle hardening to cycle softening was reduced by the increasing strain amplitude and mean strain. Cyclic hard-

ening ratio increased with increasing strain amplitude and decreased with increasing mean strain. Cyclic softening ratio increased with increasing mean strain.

2. The fatigue life in asymmetric fatigue is associated with the maximum absolute value of strain. They present a linear relationship in the double logarithmic coordinates.
3. The observation of microstructure and crack shows that crack was initiated from the void in the grains. The fatigue crack propagates through transgranular propagation. The dislocation pileup exerted a strengthening effect on the grain boundaries to prevent crack growth along the grain boundary.
4. Analysis of fracture surface shows that the different mean strains can affect the morphology of fatigue striation.

Acknowledgments

This work was supported by the National Natural Science Foundation of China under Contact No. 51574278.

References

1. X. Zhu, S. Liu, and H. Tong, Plastic Limit Analysis of Defective Casing for Thermal Recovery Wells, *Eng. Fail. Anal.*, 2013, **27**, p 340–349
2. S. Liu, H. Zheng, X. Zhu, and H. Tong, Equations to Calculate Collapse Strength of Defective Casing for Steam Injection Wells, *Eng. Fail. Anal.*, 2014, **42**, p 240–251
3. J. Wu and M. Knauss, Casing Temperature and Stress Analysis in Steam-Injection Wells, *International Oil & Gas Conference and Exhibition in China*, Society of Petroleum Engineers, 2006
4. Z.-H. Yu, L.-Y. Wang, and D.-W. Liu, Investigation on Production Casing in Steam-Injection Wells and the Application in Oilfield, *J. Hydrodyn. Ser. B*, 2009, **21**(1), p 77–83
5. H. Gu, L. Cheng, S. Huang, B. Bo, Y. Zhou, and Z. Xu, Thermophysical Properties Estimation and Performance Analysis of Superheated-Steam Injection in Horizontal Wells Considering Phase Change, *Energy Convers. Manag.*, 2015, **99**, p 119–131
6. X. Yang, Y. Yan, J. Wang, Z. Xu, and X. Yan, Strain Design and Experimental Study of Casing in Thermal Recovery Well Based on the Elastic-Plastic Constitutive Model, *Pipelines 2013: Pipelines and Trenchless Construction and Renewals—A Global Perspective*, 2013, p 1492–1500
7. L.J. Han, J.H. Jia, and Z.L. Yan, A Casing Design Method Based on Strain Variations for Wells in Thermal Recovery Processes, *J. China Univ. Pet.*, 2014, **38**(3), p 68–72
8. J. Ahmad, J. Purbolaksono, and L.C. Beng, Thermal Fatigue and Corrosion Fatigue in Heat Recovery Area Wall Side Tubes, *Eng. Fail. Anal.*, 2010, **17**(1), p 334–343
9. E. Poursaeidi and H. Bazvandi, Effects of Emergency and Fired Shut Down on Transient Thermal Fatigue Life of a Gas Turbine Casing, *Appl. Therm. Eng.*, 2016, **100**, p 453–461
10. I. Nikulin, T. Sawaguchi, A. Kushibe, Y. Inoue, H. Otsuka, and K. Tsuzaki, Effect of Strain Amplitude on the Low-Cycle Fatigue Behavior of a New Fe-15Mn-10Cr-8Ni-4Si Seismic Damping Alloy, *Int. J. Fatigue*, 2016, **88**, p 132–141
11. I. Nikitin and M. Besel, Correlation Between Residual Stress and Plastic Strain Amplitude During Low Cycle Fatigue of Mechanically Surface Treated Austenitic Stainless Steel AISI, 304 and Ferritic–Pearlitic Steel SAE 1045, *Mater. Sci. Eng. A*, 2008, **491**(1-2), p 297–303
12. D.R. Carter, W.E. Caler, D.M. Spengler, and V.H. Frankel, Fatigue Behavior of Adult Cortical Bone: The Influence of Mean Strain and Strain Range, *Acta Orthop. Scand.*, 1981, **52**(5), p 481–490
13. S.S. Manson, Interface Between Fatigue, Creep and Fracture, *Int. J. Fract.*, 1966, **2**(1), p 327–363
14. S. Sankaran, V.S. Sarma, and K.A. Padmanabhan, Low Cycle Fatigue Behavior of a Multiphase Microalloyed Medium Carbon Steel: Comparison Between Ferrite–Pearlite and Quenched and Tempered Microstructures, *Mater. Sci. Eng. A*, 2003, **345**(1-2), p 328–335
15. M. Sauzay and L.P. Kubin, Scaling Laws for Dislocation Microstructures in Monotonic and Cyclic Deformation of FCC Metals, *Prog. Mater. Sci.*, 2011, **56**(6), p 725–784
16. M.F. Giordana, P.F. Giroux, I. Alvarez-Armas, M. Sauzay, A. Armas, and T. Kruml, Microstructure Evolution During Cyclic Tests on EUROFER 97 at Room Temperature. TEM Observation and Modeling, *Mater. Sci. Eng. A*, 2012, **550**, p 103–111
17. M.N. Batista, M.C. Marinelli, S. Hereñú, and I. Alvarez-Armas, The Role of Microstructure in Fatigue Crack Initiation of 9-12%Cr Reduced Activation Ferritic–Martensitic Steel, *Int. J. Fatigue*, 2015, **72**, p 75–79
18. R. Wan, *Advanced Well Completion Engineering*, 3rd ed., Elsevier Inc, Oxford, UK, 2011, p 221–294
19. Institution BS, *Iso/cd 12106—Metallic Materials—Fatigue Testing Axial Strain—Controlled Method*, 2003
20. Z. Shen, R.H. Wagoner, and W.A.T. Clark, Dislocation Pile-Up and Grain Boundary Interactions in 304 Stainless Steel, *Scr. Metall.*, 1986, **20**(6), p 921–926
21. D. Kiener, C. Motz, W. Grosinger, D. Weygand, and R. Pippan, Cyclic Response of Copper Single Crystal Micro-Beams, *Scr. Mater.*, 2010, **63**(5), p 500–503
22. A. Nieslony, C.E. Dsoki, H. Kaufmann, and P. Krug, New Method for Evaluation of the Manson–Coffin–Basquin and Ramberg–Osgood Equations with Respect to Compatibility, *Int. J. Fatigue*, 2008, **30**(10-11), p 1967–1977
23. K. Shimada, J. Komotori, and M. Shimizu, The Applicability of the Manson–Coffin Law and Miner’s Law to Extremely Low Cycle Fatigue, *Trans. Jpn. Soc. Mech. Eng. Part A*, 1987, **53**(491), p 1178–1185
24. H. Hao, D. Ye, and C. Chen, Strain Ratio Effects on Low-Cycle Fatigue Behavior and Deformation Microstructure of 2124-T851 Aluminum Alloy, *Mater. Sci. Eng. A*, 2014, **605**, p 151–159
25. X. Wei, S.C. Wong, and S. Bandaru, A Semi-empirical Unified Model of Strain Fatigue Life for Insulation Plastics, *J. Mater. Sci.*, 2010, **45**(2), p 326–333
26. L. Lin, X. Li, J. Tan, and J. Zhang, Ultrasonic Power Spectral Analysis for Heat Treatment Transformation Products in GCr15SiMn Steel, *Trans. Mater. Heat Treat.*, 2002, **04**, p 21–24+73
27. J.G. Liu, M.W. Fu, and W.L. Chan, A Constitutive Model for Modeling of the Deformation Behavior in Microforming with a Consideration of Grain Boundary Strengthening, *Comput. Mater. Sci.*, 2012, **55**(55), p 85–94
28. L. Wang, Q. Liu, and S. Shen, Effects of Void–Crack Interaction and Void Distribution on Crack Propagation in Single Crystal Silicon, *Eng. Fract. Mech.*, 2015, **146**, p 56–66
29. X.L. Xu and R.K.N.D. Rajapakse, Analytical Solution for an Arbitrarily Oriented Void/Crack and Fracture of Piezoceramics, *Acta Mater.*, 1999, **47**(47), p 1735–1747
30. S.Y. Liu and I.W. Chen, Fatigue of Yttria-Stabilized Zirconia: II. Crack Propagation, Fatigue Striation, and Short Crack Behavior, *J. Am. Ceram. Soc.*, 1991, **74**(6), p 1206–1216